Forced convection around horizontal tubes bundles of a heat exchanger using a two-phase mixture model: Effects of nanofluid and tubes Configuration

Mohammad Tahmasebiboldaji [a], Masoud Afrand [a], Azeez A. Barzinjy [b,c], Samir M. Hamad [d,e], Pouyan Talebizadehsardari [f,g,*]

[a] Department of Mechanical Engineering, Najafabad Branch, Islamic Azad University, Najafabad, Iran
[b] Physics Education Department, Tishk International University TIU, Erbil, Kurdistan Region, Iraq
[c] Physics Department, College of Education, Salahaddin University-Erbil, Kurdistan Region, Iraq
[d] Computer Department, Cihan University-Erbil, Iraq
[e] Scientific Research Centre, Soran University, Soran, Erbil, Iraq
[f] Department for Management of Science and Technology Development, Ton Duc Thang University, Ho Chi Minh City, Vietnam
[g] Faculty of Applied Sciences, Ton Duc Thang University, Ho Chi Minh City, Vietnam

ARTICLE INFO

ABSTRACT

In this paper, numerical simulation of laminar flow and heat transfer of nanofluid on a group of heat exchanger tubes is described. For better prediction of the behavior of the nanofluid flow on the tube arrays, two-phase mixture model was used. To achieve this aim, heat transfer and laminar flow of two-phase nanofluid as cooling fluid at volume fraction of 0, 2, 4, and 6% solid nanoparticles of silver and Reynolds numbers of 100 to1800 were investigated for different Configurations of tube arrays. The results indicated when the nanofluid collides with the tube arrays, the growth of heat boundary layer and gradients increase. The increase in the growth of boundary layer in the area behind the tubes was very remarkable, such that at the Reynolds number of 100, due to diffusion of the effect of wall temperature in the cooling fluid close to the wall, it had a considerable growth. Further, from the second row onwards, the slope of pressure drop coefficient diagrams was descending. Among the different Configuration s of tubes and across all the investigated Reynolds numbers, square Configuration had the maximum pressure drop coefficient as well as the highest extent of fluid momentum depreciation.

1. Introduction

In recent decades, to save energy consumption and raw materials and considering economic and environmental issues, great attempts have been made to develop efficient heat exchange devices. The global demand for efficient, reliable, and economical heat exchanger devices especially in process industries, power generation, cooling and air conditioning systems, heat exchangers, vehicles, and plant instruments is rapidly increasing [1–3]. Heat transfer efficiency in equipment such as heat exchangers, the heat conductivity of the energy carrying fluid, and convection heat transfer coefficient play a significant role. Considering usage of conventional and typical cooling fluids including water, oils, and ethylene, with the increased global competition across different industries and the role of energy in production costs, these industries are progressively moving towards development of advanced and new fluids with high thermal indices such as nanofluids. Many researchers in heat transfer science have dealt with the investigation of the flow behavior and heat transfer across different geometries and dimensions [4–8]. In the majority of these studies, the effect of elevated heat transfer with new cooling fluids has been reported. By employing these fluids in industrial instruments such as heat exchangers, their thermal efficiency can be enhanced. In this regard, applied studies have been conducted by researchers. The studies on investigation of flow on tube arrays include experimental and numerical studies. Kim [9] dealt with numerical investigation of flow on tube arrays with different Configurations. He found that the changes in the step of tubes have a great impact on frictional drag and local Nusselt number. Iwaki et al. [10] dealt with experimental investigation of the ratio of different dimensions of tube arrays in two special Configurations: linear and staged by particular image velocimetry (PIV) method. Their experimental results indicated that the structure of flow field in the tube arrays is dependent on velocity vector field, intensity of turbulence, and structure of vortexes. Godson et al.

[11] experimentally investigated heat transfer characteristics in shell and tube heat exchanger using water-silver oxide nanofluid. The results of their research indicated that with the increase in the volume fraction of solid nanoparticles, the efficiency and convection heat transfer coefficient increase, with the maximum convection coefficient and efficiency reported as 12.5 and 6.14%, respectively. Wang et al. [12] examined laminar and turbulent flow of air on tube arrays in different Configurations. In this research, they studied the flow properties and heat transfer of air flow at Reynolds numbers of 100 and 300. The results indicated that heat transfer in the first tube in each row is the lowest in comparison with other tubes in that row. Further, hydrodynamic properties and heat transfer in the first tube are almost the same in the investigated Configurations. Chidanand et al. [13] dealt with numerical and experimental examination of air flow on tube arrays with an integral splitter plate. Their research was performed within the Reynolds numbers of 5500–14,500. They found that use of the splitter plate in the trail of tubes results in increased Nusselt number for the fluid flow. Further, use of a plate connected to tubes causes increased heat transfer and thermal-fluid efficiency with decrease in pressure drop in comparison with typical tube arrays. The maximum increase in thermal-fluid performance is 60–82% at Reynolds number of 5500. Wang et al. [14] dealt with numerical investigation of heat transfer behavior of water fluid in shell and tube heat exchangers. They found that change in the degree of slope of tubes has no significant effect on fluid flow properties and heat transfer for liquid flow across the entire tube Configuration. Iacovides et al. [15] examined and simulated flow on tube arrays using numerical method. In their research, the distance between tubes was studied in linear (rectangular) Configuration of tube arrays. They found that the pathway of fluid flow between tubes will differ based on the extent of turbulence. Mangrulkar et al. [16] dealt with numerical investigation of flow and friction factor of air fluid on tube arrays with a Cam section within the Reynolds range of 11,500–42,500. They observed that thermal-fluid efficiency in tube arrays with a Cam section is greater than in those with circular cross section. Moreover, friction factor in this type of cross section diminishes by 85–89% in comparison with circular cross section.

In this research, for the first time, laminar and two-phase flow of water-silver nanofluid is investigated numerically on tube arrays with a circular cross section with different Configurations. Use of nanofluids and simulation of flow and heat transfer in a two-phase form, investigation of different Configurations of tube arrays, concurrent comparison of parameters including Nusselt number, friction factor, pressure drop, dynamic pressure drop coefficient and the forces exerted on the tube arrays for different Reynolds ranges and volume fraction of solid nanoparticles make this research distinct from other studies. The results of this investigation can be practically used in cooling systems of tube bundles which are an important part of nuclear power plants, shell & tube heat exchangers and Spacecraft.

2. Problem statement (description of dimensional physics)

In this research, simulation of Nusselt number and laminar heat transfer of nanofluid on tube arrays of heat exchanger is described. Fig. 1-a depicts a schematic drawing of the problem of interest. It is seen that the geometry consists of three parts including the inlet region, the inner region, and the outlet region. The inlet region is considered to guarantee a fully developed flow, while the outlet region is considered to avoid any backflow into the test section. In this research, the studied geometry and Configuration of tube arrays have been described by Equilateral Triangle (ET), Equal Spacing (ES), and Rotated Square (RS) Configurations, according to Fig. 1-b.

Fig. 1-b demonstrates the Configuration associated with the tube arrays studied in this research. The dimensions of the studied geometry include input length L_{us}, middle length L_{tb}, and output length L_{ds}, and d (tube diameter). The dimensions of the studied geometry is reported in Table 1. In this research, the heat transfer and laminar flow behavior

Table 1
Dimensions of the studied geometry.

Tube diameter (d)	2 cm
Input length (L_{us})	20 cm
Output length (L_{ds})	15 cm
ET Configuration	$S_T = 10$ cm $S_D = 10$ cm $S_L = 8.66$ cm
ES Configuration	$S_T = 10$ cm $S_D = 10$ cm $S_L = 10$ cm
RS Configuration	$S_T = 10$ cm $S_D = 7.07$ cm $S_L = 5$ cm

Table 2
The thermophysical properties of the base fluid and solid nanoparticles [17,18].

Material	Pr	ρ (kg/m^3)	C_p (J/kgK)	k (W/mK)
Pure water	6.2	997.1	4179	0.613
Silver oxide	–	10,500	235	429

of the two-phase nanofluid as the cooling fluid is examined at volume fraction of 0,2,4, and 6% solid silver nanoparticles along with Reynolds numbers of 100, 400, 1000, and 1800. The extent of heat flux exerted to the wall of tubes is $q" = 6000$ W/m^2. The temperature of the input fluid is 293 K, and diameter of the solid nanoparticles is considered 10 nm. The properties of the silver nanoparticles and water base fluid are considered according to Table 2.

Triangle (ET), Equal Spacing (ES), and Rotated Square (RS) Configurations, according

The aim of this research is investigation of heat transfer and flow of two-phase nanofluid across different tube array Configurations and comparing flow parameters with each other. In this study, the fluid flow is considered laminar, two-phase, and Newtonian, and radiation effects are neglected. All simulations of heat transfer and fluid flow are performed through two-phase mixture method.

3. The governing equations and assumptions

3.1. Equations of two-phase and laminar flow of nanofluid

The equations governing two-phase and laminar flow of the nanofluid include continuity equations, momentum equations, and energy equation [19].

$$\nabla.(\rho_m \vec{V}_m) = 0 \tag{1}$$

$$\vec{V}_m = \frac{\sum_{Z=1}^{n} \varphi_Z \rho_Z \vec{V}_Z}{\rho_m} = V_Z \tag{2}$$
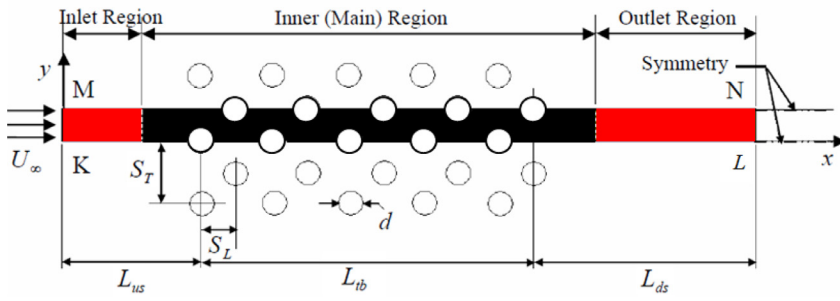
$$\rho_m = \sum_{Z=1}^{n} \varphi_Z \rho_Z \tag{3}$$

$$\nabla.(\rho_m \vec{V}_m \vec{V}_m) = -\nabla P_m + \nabla.\left[\mu_m\left(\nabla \vec{V}_m + \nabla \vec{V}_m^T\right)\right] \tag{4}$$
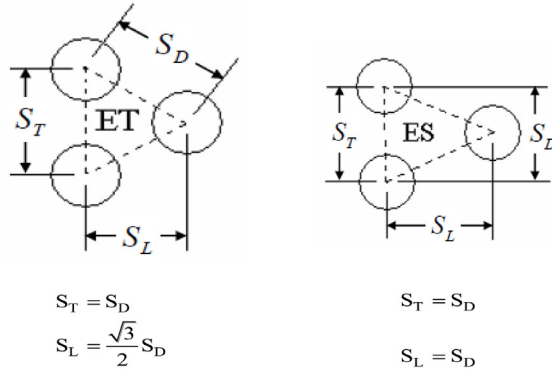
$$\vec{V}_{dr,Z} = \vec{V}_Z - \vec{V}_m \tag{5}$$

$$\mu_m = \sum_{Z=1}^{n} \varphi_Z \mu_Z \tag{6}$$

$$\nabla \cdot (\rho_m h_m \vec{V}_m) + \nabla \cdot (P\vec{V}_m) = \nabla.(k_m \nabla T) \tag{7}$$

$$\rho_m h_m = \sum_{Z=1}^{n} (\varphi_Z \rho_Z h_Z), \quad k_m = \sum_{Z=1}^{n} \varphi_Z (k_Z) \tag{8}$$

Fig. 1. (a) schema of the studied geometry and (b) the Configurations of tube arrays in this research.

In the above equations, V_m is the mean velocity (bulk) of the mixture, $V_{dr,z}$ is the driving velocity of the secondary phase z, and indices T, P, φ, μ, and ρ are temperature, pressure, volumetric fraction, dynamic viscosity, and density, respectively. In Eqs. (1)–(8), the subscripts of z, dr, and m represent the secondary phase z, driving force, and mixture (solid-liquid phases), respectively. The equations used for calculation of thermophysical properties of the agent nanofluid are defined as follows:

The equation for calculation of thermal conductivity of the nanofluid [20,21].

$$\frac{k_m}{k_f} = 1 + 64.7\phi^{0.764}\left(\frac{d_f}{d_{np}}\right)^{0.369}\left(\frac{k_{np}}{k_f}\right)^{0.7476}Pr^{0.9955}Re^{1.2321}$$

$$Re = \frac{\rho_f k_b T}{3\pi\mu^2 l_f}, \quad Pr = \frac{\mu_f}{\rho_f \alpha_f}, \quad \mu = A \times 10^{\frac{B}{T-C}}, \quad T = T_{in}$$

$$B = 247(K), \quad A = 2.414 \times 10^{-5}(Pa.s), \quad C = 140(K)$$

(9)

The equation for calculation of dynamic viscosity [22,23]

$$\mu_{eff} = \left(123\phi^2 + 7.3\phi + 1\right)\mu_f$$

(10)

Determination of the specific heat capacity [24]

$$(\rho C_p)_m = (1 - \phi)(\rho C_p)_f + \phi(\rho C_p)_{np}$$

(11)

Density of nanofluid [25–28],

$$\rho_m = (1 - \varphi)\rho_f + \varphi\rho_{np}$$

(12)

Dimensionless parameters are defined as follows [29,30]:

$$X = \frac{x}{d}, \quad Y = \frac{y}{d}, \quad V = \frac{v}{u_c}, \quad \theta = \frac{T - T_c}{\Delta T}, \quad U = \frac{u}{u_c}, \quad P = \frac{\bar{P}}{\rho_{nf}u_c^2}, \quad \Delta T = \frac{q_0'' d}{k_{nf}},$$

$$Pr = \frac{\vartheta_{nf}}{\alpha_{nf}}$$

(13)

Another parameter in investigating the performance of microchannel is friction factor, which is calculated by the following equation [31],

$$Cf = \frac{2 \times \tau_w}{\rho u_{in}^2}$$

(14)

Average Nusselt number is a dimensionless number and represents the heat transferred to through convection to the heat transferred
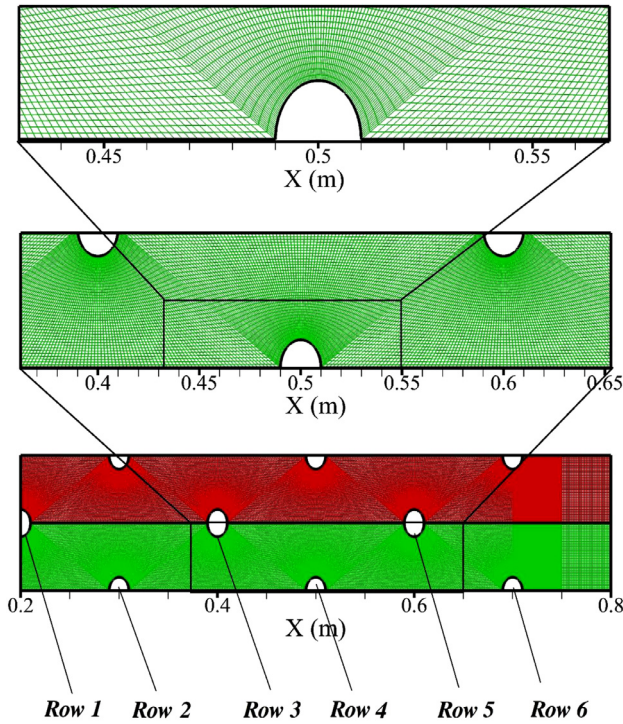
Fig. 2. Details of mesh construction.

through conduction, which is obtained by the following equation [32–34],

$$Nu_x = \frac{hd}{k_{nf}} \rightarrow Nu_{ave} = \frac{1}{L_{tb}} \int_0^{L_{tb}} Nu_x(x)dx \tag{15}$$

Pressure drop in the input and output mouse is calculated by the following equation:

$$\Delta P = P_{in} - P_{out} \tag{16}$$

Performance evaluation criterion (PEC) known as thermal-fluid efficiency is defined as follows [35],

$$PEC = \frac{\left(\frac{Nu_{ave}}{Nu_{ave,\varphi=0}}\right)}{\left(\frac{C_f}{C_{f,\varphi=0}}\right)^{(1/3)}} \tag{17}$$

The values of Reynolds number are calculated as follows [19],

$$Re = \frac{\rho_{eff} d V_m}{\mu_{eff}} \tag{18}$$

The extent of pressure drop is calculated by the following equation,

$$Cp = \frac{P - P_{out}}{\frac{1}{2} \times \rho \times u^2} \tag{19}$$

3.2. Solution assumptions

In this investigation, the nanofluid flow is assumed as forced and permanent. The nanofluid properties are assumed as constant (homogeneous) and independent of temperature, and Newtonian. The nanofluid behavior is modeled as two-phase and the numerical solution field is solved through two-phase mixture method. A constant and uniform heat flux is applied to each tube and symmetry boundary condition is used for other walls. In this research, radiation effects are neglected. The boundary condition of velocity on tubes is lack of slip. In this research, the nanofluid flow is assumed laminar, Newtonian, compressible, and two-phase. Second-order discretization [36] and SIMPLEC algorithm [37,38] are used for solving the equations governing the flow. The numerical solutions are carried out using the finite volume CFD code Fluent. The maximum residual resulting from numerical solution in the solution processes of this simulation is 10^{-6}.

4. Mesh study

In this research, for numerical simulation of the solution domain, finite volume method and rectangular structured mesh have been used. In Table 3, the number of structured meshes has changed from 15,000 to 52,500 (Fig. 2). In order to make the results independent of the number of chosen meshes, changes in the parameters of average Nusselt number, friction factor at ES state for the first row of tubes have been done at
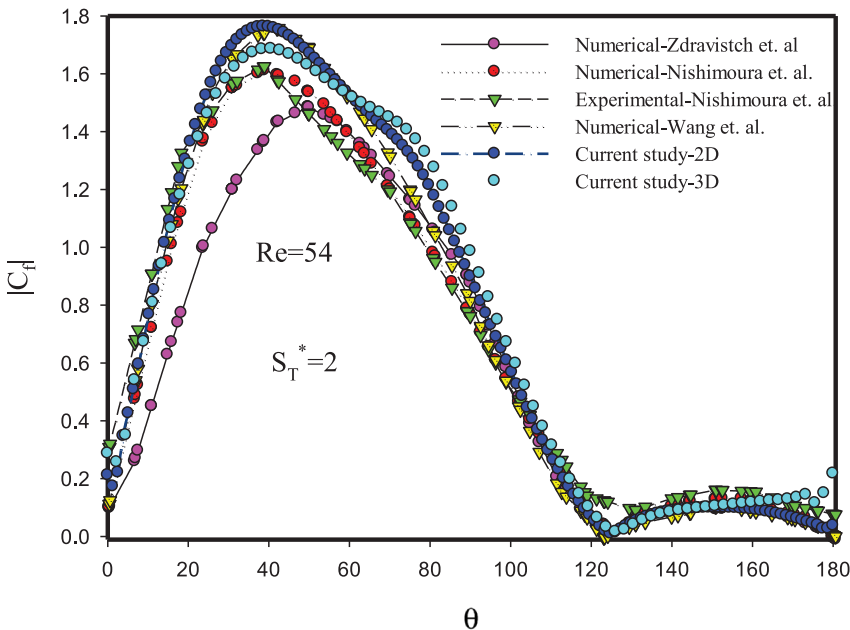

Fig. 3. Validation of this study with the study by Zdravistch [39], Nishimura [40], and Wang et al. [12].

Table 3
Study of the mesh number.

	(300 × 50)	(400 × 57)	(500 × 60)	(600 × 66)	(700 × 75)
Nu_{ave}	49.73	50.11	51.7	52.45	53.6
Difference	7.22%	6.511%	3.544%	2.145%	–
$C_{f,ave}$	0.143	0.121	0.113	0.099	0.091
Difference	57.14%	33	24.17%	8.8%	–

Reynolds number of 400 and volume fraction of 4% of nanoparticles. The results of investigation of mesh have been compared with the larger number of meshes (52,500). Considering the changes in Nusselt number and friction factor and the obtained error value, the most suitable and optimal state of mesh number is 600 × 66, as changes in Nusselt number

and average friction factor have an error below 10%. All simulations of this study are performed for tube array Configuration with 39,600 meshes.

5. Results and discussion

5.1. Validation

Fig. 3 demonstrates validation of this numerical study with the study by Zedravich [39], Nishimora [12], and Wang et al. [40]. This investigation has been performed at Reynolds number of 54 and for $S_T^* = S_T = 2$. The investigation is performed for estimation of local friction factor behavior on the tube array. The findings reveal that the mean percentage difference between our results and those obtained
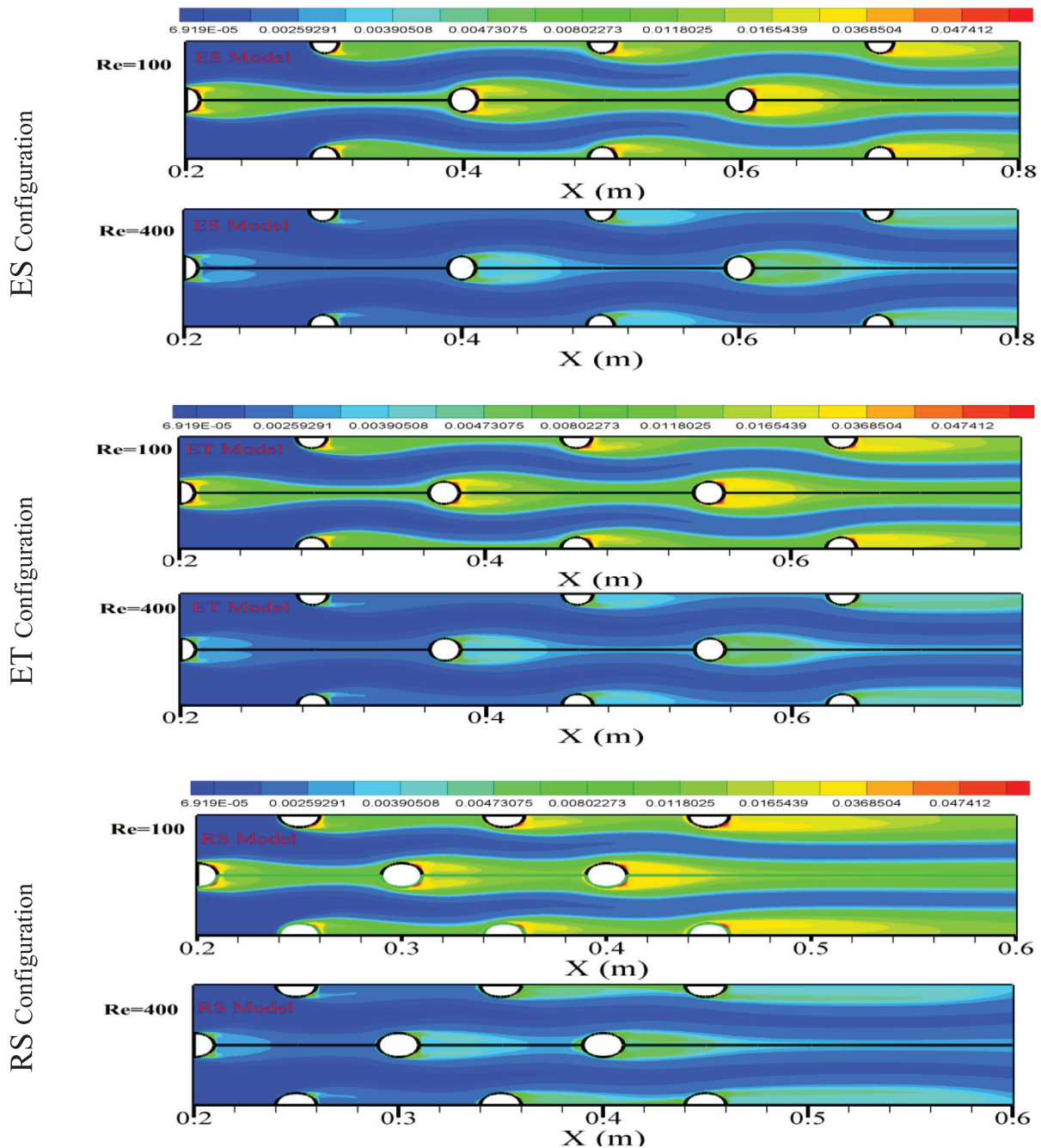

Fig. 4. Dimensionless temperature contours across different Configurations of tube arrays at volume fraction of 6% solid nanoparticles at $Re = 100$ and $Re = 400$.
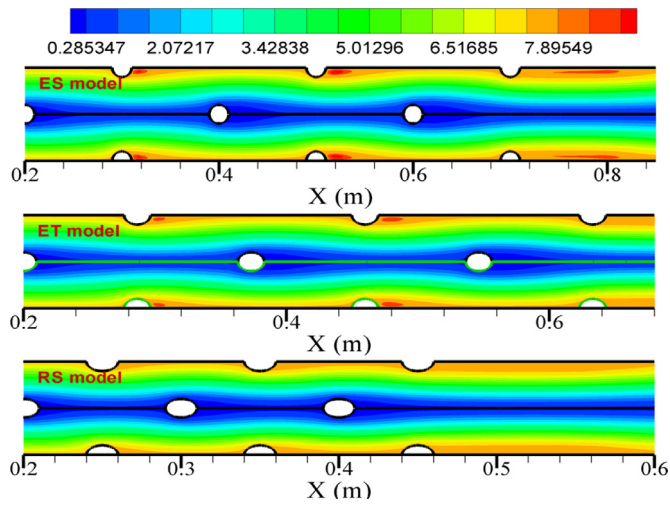
Fig. 5. The contours of streamlines across different tube array Configurations at volume fraction of 6% solid nanoparticles and Reynolds number of 1800.

by Zedravich [39], Nishimora [12], and Wang et al. [40] for two-dimensional geometry is respectively 14.45%, 7.54%, and 9.01%, while these values for the case of three-dimensional geometry are respectively 11.88%, 5.23%, and 7.77%. Considering the suitable correspondence of these numerical results with the studies conducted in this regard in two-dimensional and three-dimensional geometries, it is found that the boundary conditions and estimations considered for solving the problem enjoy a good accuracy. Selection of the numerical solution field in two-dimensional state is more suitable than three-dimensional state.

The tube surface wall shear distribution is presented using a local friction coefficient, C_f, on each tube:

$$C_f = \frac{\tau_w}{\frac{1}{2}\rho V_{max}^2} \tag{20}$$

where τ_w is the wall shear stress on the tube surface at an angle θ from the front of the tube and V_{max} is the mean velocity at the low cross-sectional area. The relationship between V_{max} and the inlet velocity, U_∞,

is [41,12]:

$$\frac{V_{max}}{U_\infty} = \max\left\{\frac{S_T^*}{S_T^*-1}, \frac{\frac{1}{2}S_T^*}{\left[\left(\frac{1}{2}S_T^*\right)^2\left(S_L^*\right)^2\right]^{1/2}-1}\right\} \tag{21}$$

In this work, only the nominal pitch ratios of 1.25 and 2.0.

### 5.2. Effects of Reynolds numbers

Fig. 4 compares dimensionless temperature contours across different Configurations of circular tube arrays at the volume fraction of 6% of solid nanoparticles. This investigation has been performed at Reynolds numbers of 100 and 400. In each Configuration of ET, ES, and RS in the tube arrays, it is observed that the temperature of the cooling fluid after entering the region in which the tube array is placed is affected by thermal gradients. Based on these contours, it is seen that the extent of thermal gradients undergoes fewer changes at Reynolds number of 400, in comparison with 100. In collision of the fluid with the tube arrays, it is observed that growth of heat boundary layer begins. This increase is more considerable at the backside of tubes, such that at Reynolds number of 100, due to diffusion of the effect of wall temperature in the cooling fluid close to the wall, it has a remarkable growth.

In Fig. 5, the contours of streamlines across different Configurations of tube arrays including ES, ET, and RS have been compared at volume fraction of 6% solid nanoparticles at Reynolds number of 1800. In investigation of the hydrodynamic behavior of the fluid flow over circular tube arrays, it is seen that velocity gradients increase dramatically. The extent of increase in the growth of velocity boundary layer with passage of fluid over the tube arrays is maximum due to formation of a weak region and instability of the velocity profile. Across the examined Configurations, in ES due to the maximum longitudinal distance between the tube arrays, after passing over the tube arrays, the fluid flow faces vortex formation, and gradually the extent of growth of vortexes behind the terminal tube arrays reaches its maximum. This behavior is caused by diminished inertia force of the fluid in comparison with viscosity forces. Furthermore, among the different studied Configurations, in RS due to the minimum longitudinal distance between the tube arrays, this state has the minimum weak region.

In Fig. 6, the diagrams of average friction factor have been plotted at volume fraction of 6% solid nanoparticles at Reynolds numbers of
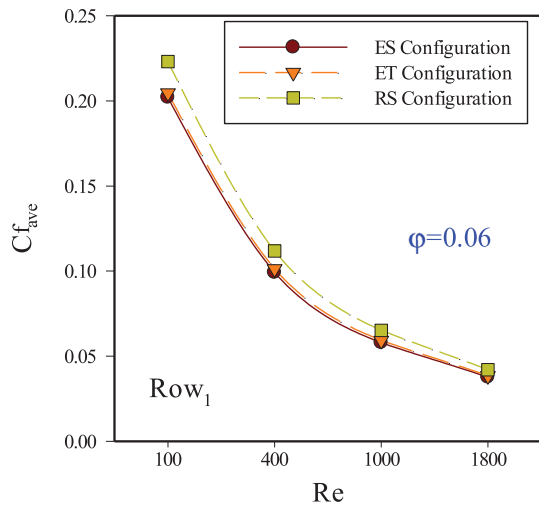
(a-6) of the first row (Row1)
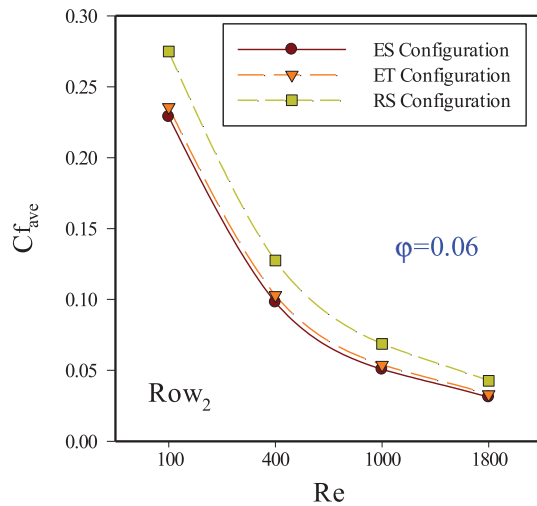
(b-6) of the second row (Row2)

Fig. 6. Average friction factor diagrams at the volume fraction of 6% solid nanoparticles at different Reynolds numbers and Configurations of tube arrays on tube arrays.
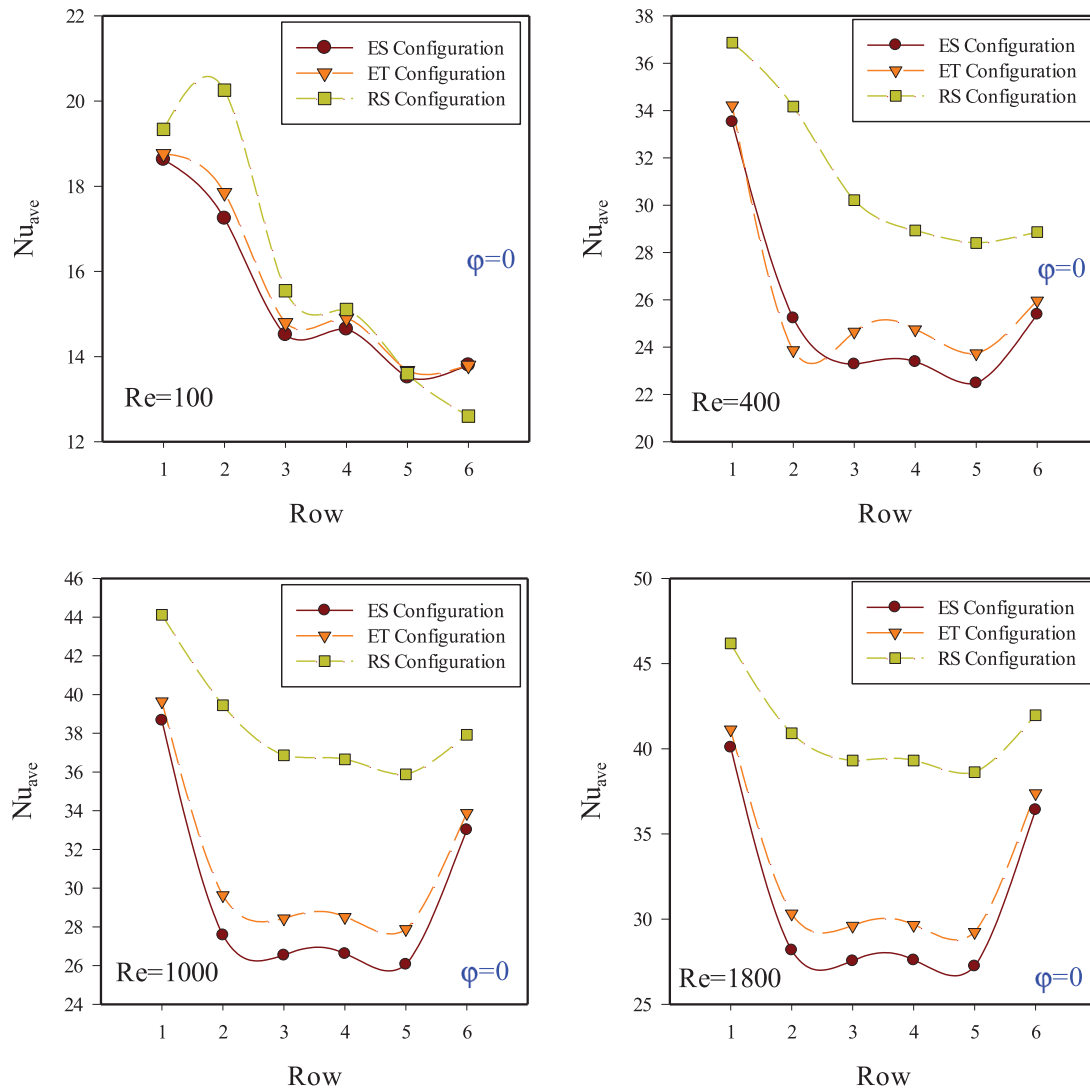
Fig. 7. Changes in average Nusselt number across different rows of the tube arrays for the cooling fluid of pure water.

100–1800 for tube arrays (a-6) of the first row (Row$_1$) and (b-6) of the second row (Row$_2$). Considering the diagrams in Fig. 6, the extent of changes in the average friction factor is dependent on the fluid velocity. With the increase in Reynolds number in the first and second rows of the tube arrays, friction factor declines. Indeed, the friction factor is a criterion representing changes in the velocity elements on the tube wall, which is a result of changes in the fluid momentum. At Reynolds 100, due to dominance of the effects of viscosity forces on the tube arrays, friction factor is maximum. At Reynolds 1800, however, due to increased fluid velocity and developed inertia forces against viscosity forces, the friction factor declines significantly. In investigation of friction factor diagrams, it can be stated that the Configuration of tubes which has the minimum longitudinal step has the maximum friction factor. On the other hand, the Configurations with the maximum longitudinal step have the lowest friction factor. Among the studied Configurations, friction factor is larger in the tubes of the second row in comparison with the first row, which is most of you to diminished fluid velocity in the second row, when compared with the first row.

Figs. 7 and 8 represent the average Nusselt number at volumetric fractions of 0 and 6% solid nanoparticles in rows a-6 of tube arrays at Reynolds numbers of 100–1800. This investigation has been performed for every Configuration, ES, RS, and ET. In investigation of average Nusselt number on tube arrays with different Configurations and volumetric fractions of solid nanoparticles, based on the mentioned diagrams, it is observed that elevation of Reynolds number causes increased convection heat transfer coefficient, which in turn brings about elevation of Nusselt number. Changes in the geometrical position of placement of tube arrays are also important in increasing average Nusselt number, such that in the Configurations of tubes, with decrease in the longitudinal distance between them, as velocity gradients grow significantly in these regions, it can develop a better mixing in the cooling fluid. Further, given the plotted diagrams, with increase in the volume fraction of solid nanoparticles, average Nusselt number increases. Presence of solid nanoparticles in the cooling fluid causes improved Brownian motion and give them movement of particles in the cooling bed, it can displace a volume of the fluid, causing removal of heat flux in warm regions,
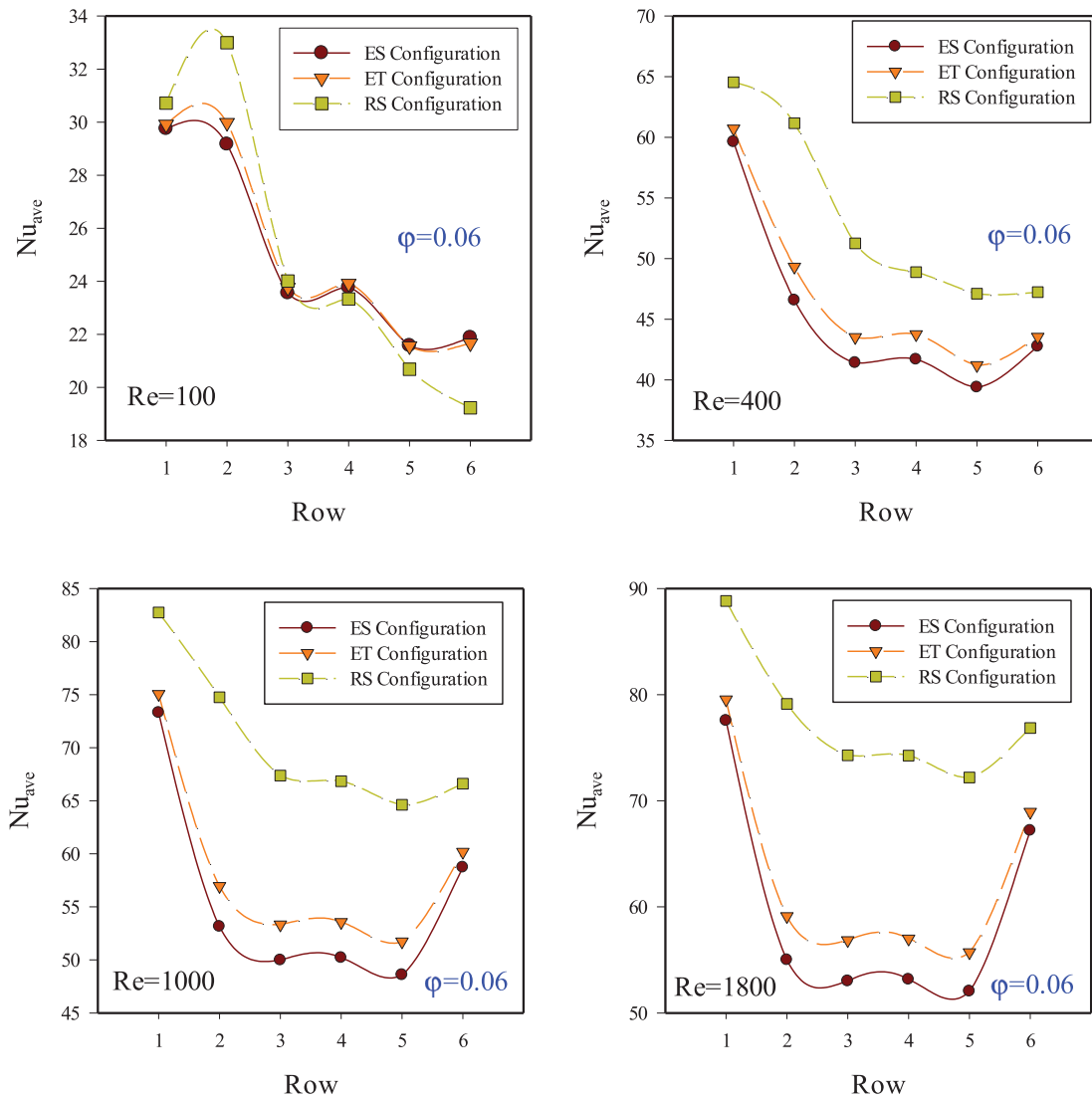
Fig. 8. Changes in average Nusselt number across different rows of tube arrays for the volume fraction of 6% solid nanoparticles at different Reynolds number.

thereby increasing heat transfer, as with other micron mechanisms of heat transfer. With increase in solid nanoparticles, due to reduction in the thickness of heat boundary layer and increased collision of particles with warm surfaces and improved heat conductivity mechanism in the cooling fluid, the extent of heat transfer coefficient increases significantly.

Among the different Configurations of tube arrays, it can be stated that across all Reynolds numbers especially 400–1800, RS type can cause a remarkable increase in average Nusselt number. This means that the diagrams of average Nusselt number of this type of Configuration have the maximum level when compared with other Configurations. In ES and ET, Nusselt number has the lowest level. In investigation of changes in the average Nusselt number on rows a–6, it can be stated that the first row has the maximum average Nusselt number and gradually until the fifth through, the extent of heat transfer over each tube array diminishes. This is mainly due to a significant growth in velocity and heat boundary layer due to separation of flow on the surface

of tubes after the first row. From the fifth row onwards, especially at the sixth row, average Nusselt number increases again to an acceptable extent, which is due to full mixing of the cooling fluid due to placement of rows ahead in the fluid path. At Reynolds 100 and in ES in the sixth row, the minimum heat transfer occurs, while the maximum heat transfer is associated with the second row of tubes. At Reynolds 400–1800, for all volumetric fractions of solid nanoparticles, the behavior of changes in the average Nusselt number on the tube arrays seems to be almost the same. In Fig. 8, due to existence of the maximum volume fraction of solid nanoparticles, maximum levels are observed in these diagrams.

5.3. Effects of fractions of solid nanoparticles

Fig. 9 reveals angular changes in local Nusselt number on the first row (Row$_1$) at Reynolds number of 400. In this figure, changes in Nusselt number have been plotted for angles 0–180° Considering the
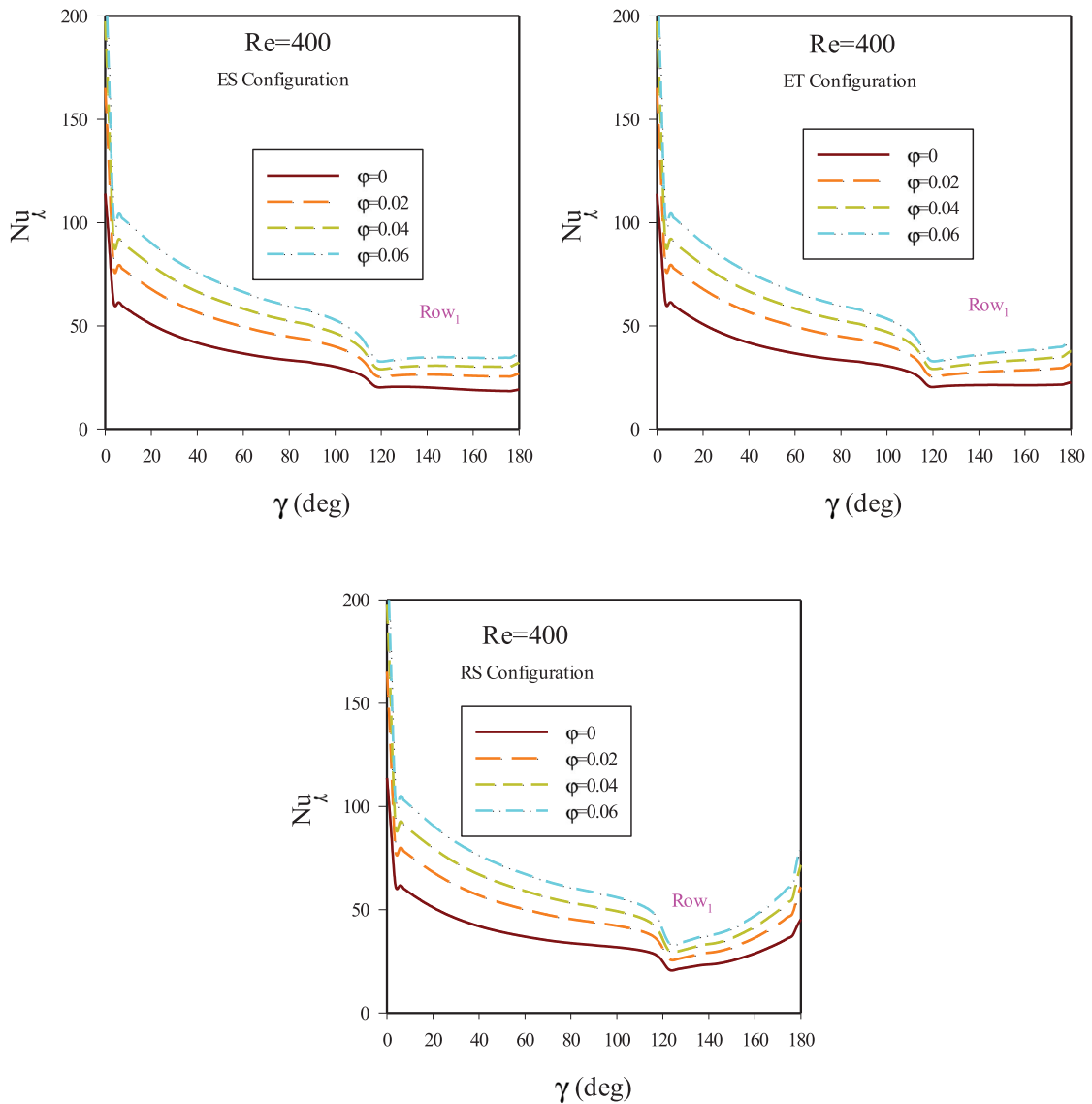
Fig. 9. The diagrams of local Nusselt number at Reynolds 400, on the tube arrays of the first row (Row$_1$).

diagrams of local Nusselt number which have been plotted for different Configurations of tube arrays and different volumetric fractions of solid nanoparticles, it is seen that in collision of the fluid with the circular surface of tube arrays, the extent of heat transfer undergoes some changes due to angular coordinates. Across all diagrams of Fig. 9, it is seen that when fluid collides with the circular surface on tubes, Nusselt number reaches its maximum, which is due to the maximum difference of the temperature of surface and fluid. Once the fluid passes over 0–120° regions, the extent of heat transfer diminishes due to changes in the velocity elements on the circular surface. At 120°, due to separation of the fluid flow off the circular surface and instability of velocity profile, some special changes are observed in the behavior of local Nusselt number. The fluid movement after 120° until 180° brings about increased heat transfer due to formation of weak region and mixing of the fluid vortex resulting from pressure drop at the backside of the tube arrays.

In Fig. 10, changes in the local friction factor have been plotted in angular path of fluid motion on the second row at Reynolds 100 at volume fraction of 0–6% solid nanoparticles. Considering the diagrams of local friction factor on the circular path of tubes in the second row, it can be stated that with the movement of fluid over this path, the velocity elements have continuously different changes. At Reynolds 100, it is observed that with the movement of fluid over the second row of tubes, local friction factor begins to increase. This extent of growth reaches its maximum at 60°, after which until 120°, it diminishes continuously. At 120°, due to separation of the fluid off the surface, changes in the local friction factor decreased significantly on the surface of the second row of tubes. Local friction factor after 120° until 180° has a primary ascending trend and then descending trend. Among the investigated diagrams, elevation of the volume fraction of solid nanoparticles is followed by elevated friction factor. This is mainly due to increased viscosity and density of the fluid, such that a fluid with higher density and
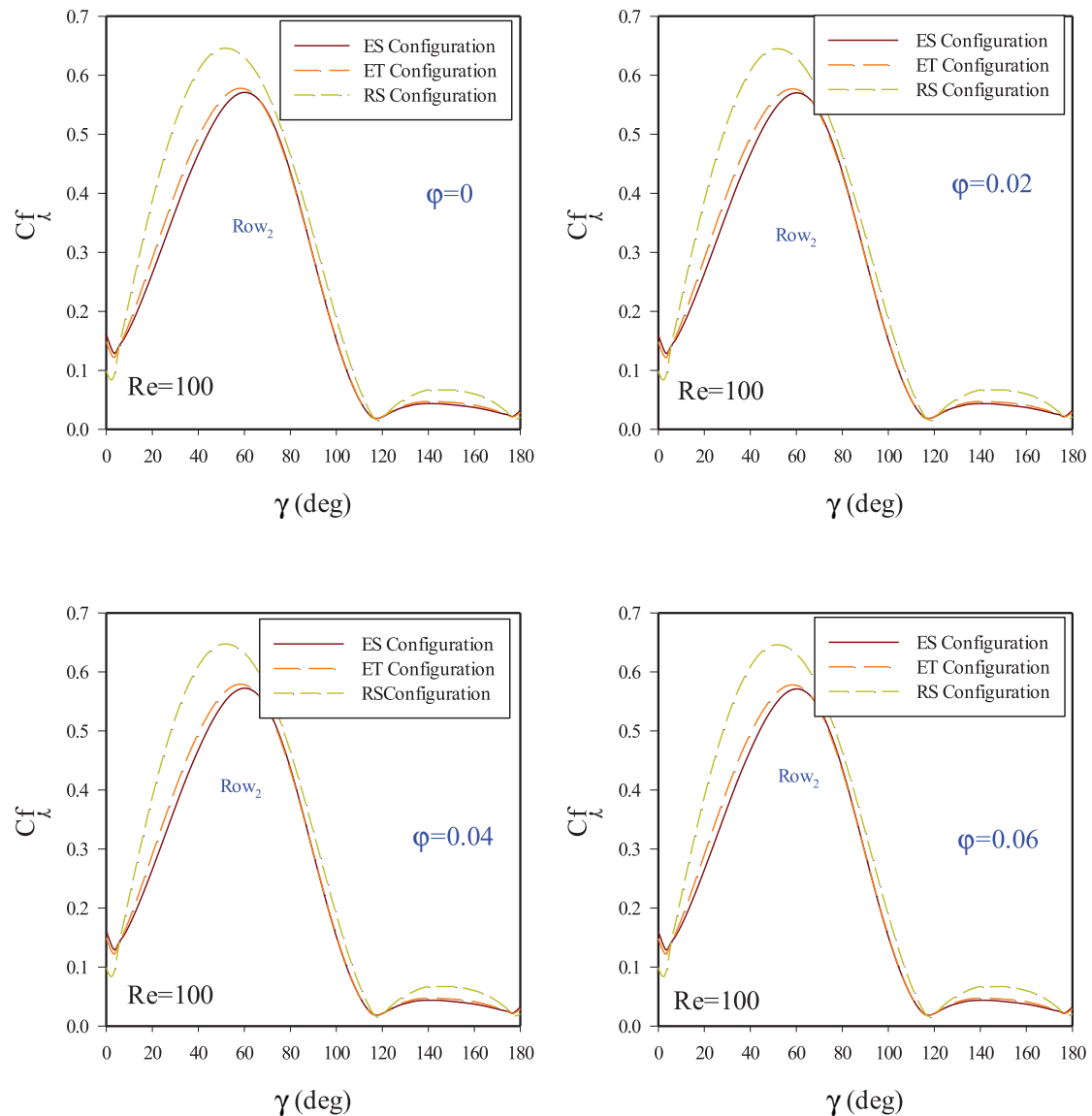
Fig. 10. The diagrams of local friction factor on the second row of tubes at Reynolds 100 and different solid volume fractions.

viscosity has a greater contact with the surface of tubes, bringing about increased friction factor. Among the Configurations, it is seen that in RS Configuration, the extent of local friction factor reaches its maximum. On the other hand, in ET and ES, local friction factor has a lower value respectively, and their trend is almost the same. Note that in RS, the maximum value of local friction factor occurs at an angle between 40 and 60°. However, this occurs at around 60° for the two other Configurations. Across all the investigated Configurations at Reynolds 100, fluid separation off the surface occurs at 120°, which has been reported for laminar flow in many studies. Considering the diagrams in Fig. 11, the extent of local friction factor on the second row has been shown at Reynolds 1000. With the increase in the fluid velocity, the extent of fluid separation angle off the surface and maximum friction factor happen at an angle different from that of Reynolds 100. It is observed that at Reynolds 1000, for ES, the extent of maximum friction factor occurs at around 60°, while occurring at 80° for ES and ET. Comparing

diagrams in Figs. 10, 11 and Table 4. it is observed that with elevation of Reynolds number, friction factor diminishes significant and the levels of diagrams of local friction factor also diminish considerably. In Fig. 11, Table 4. across all volumetric fractions of solid nanoparticles and all Configurations of the tube arrays, the extent of fluid separation occurs at 130° which is due to increased momentum (elevated inertial force versus viscosity force) of the fluid at Reynolds 1000 in comparison with 100. Following separation of the fluid, the behavior of the local friction factor on the second rule of tubes has two maximum points, occurring at 140° and 160°, respectively (Table 4.). This is due to development of a weak region and strong velocity gradients at Reynolds 100 in comparison with 100. These changes are very evident for RS Configuration.

Fig. 12 represents changes in the static pressure along MN line across different Configurations of tube arrays and volume fraction of 0–6% solid nanoparticles. This investigation has been described to explain
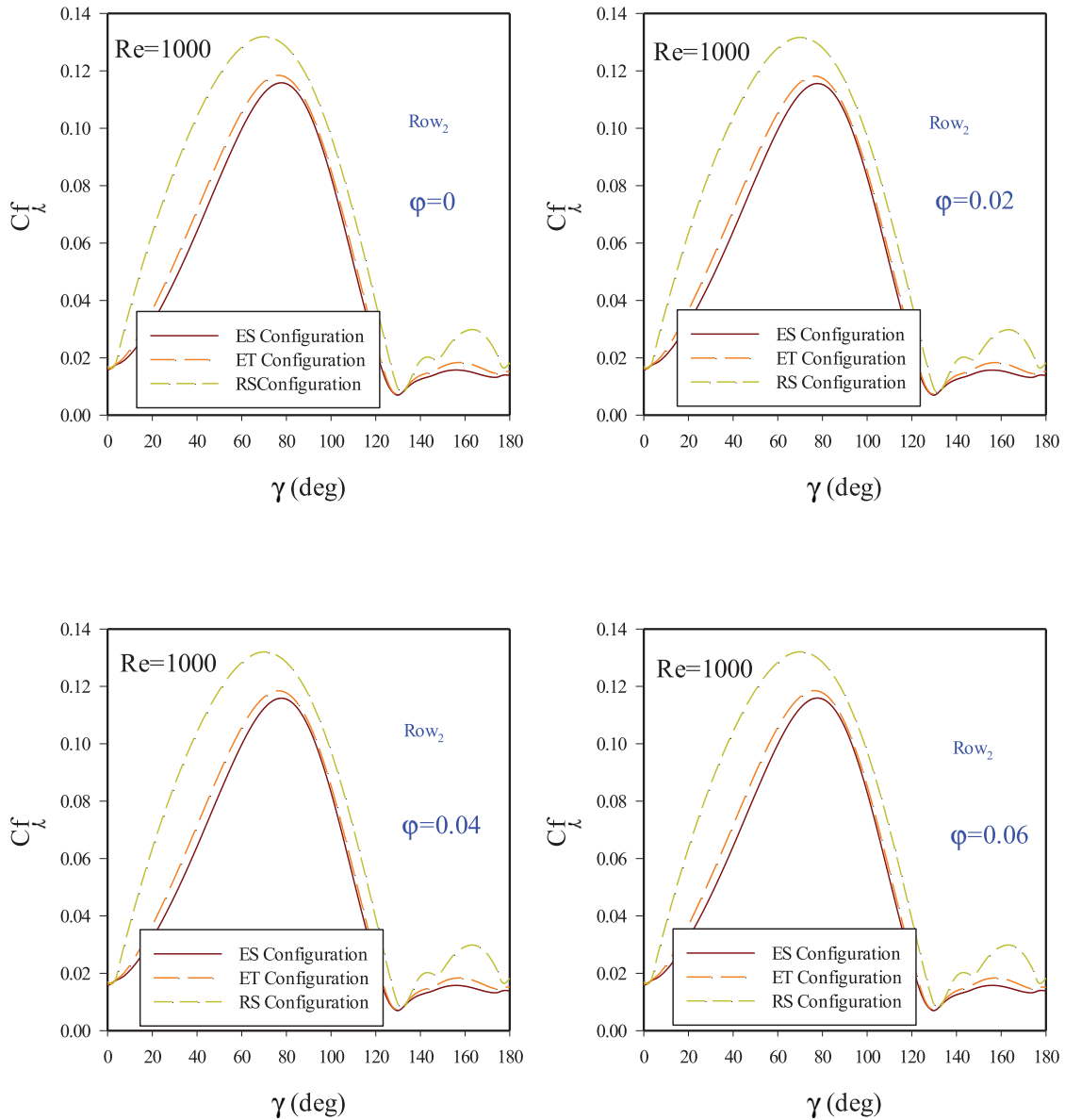
Fig. 11. The diagrams of local friction factor on the second row of tubes at Reynolds 1000 and different solid volume fractions.

Table 4
The variations of C_{fAve} in different Reynolds number and different solid volume fractions.

| Reynolds number Configurations volume fraction of nanoparticles	$Re = 1000$			$Re = 100$		
	ES	ET	RS	ES	ET	RS
$\phi = 0.0$	5.103	5.420	6.910	23.063	23.744	27.714
$\% \ C_{f \ Ave} = \frac{C_{f \ Ave \ \varphi=0.0} - C_{f \ Ave \ \varphi=0.0}}{C_{f \ Ave \ \varphi=0.0}}$	0	0	0	0	0	0
$\phi = 0.02$	5.115	5.432	6.923	23.099	23.781	27.754
$\% \ C_{f \ Ave} = \frac{C_{f \ Ave \ \varphi=0.02} - C_{f \ Ave \ \varphi=0.0}}{C_{f \ Ave \ \varphi=0.0}}$	0.23%	0.18%	0.18%	0.15%	015%	0.14%
C_{fAve} $\phi = 0.04$	5.116	5.433	6.925	23.109	23.791	27.766
$\% \ C_{f \ Ave} = \frac{C_{f \ Ave \ \varphi=0.04} - C_{f \ Ave \ \varphi=0.0}}{C_{f \ Ave \ \varphi=0.0}}$	0.25%	0.23%	0.21%	0.19%	0.19%	0.18%
$\phi = 0.06$	5.118	5.435	6.928	23.159	23.843	27.821
$\% \ C_{f \ Ave} = \frac{C_{f \ Ave \ \varphi=0.06} - C_{f \ Ave \ \varphi=0.0}}{C_{f \ Ave \ \varphi=0.0}}$	0.29%	0.27%	0.26%	0.41%	0.41%	0.38%
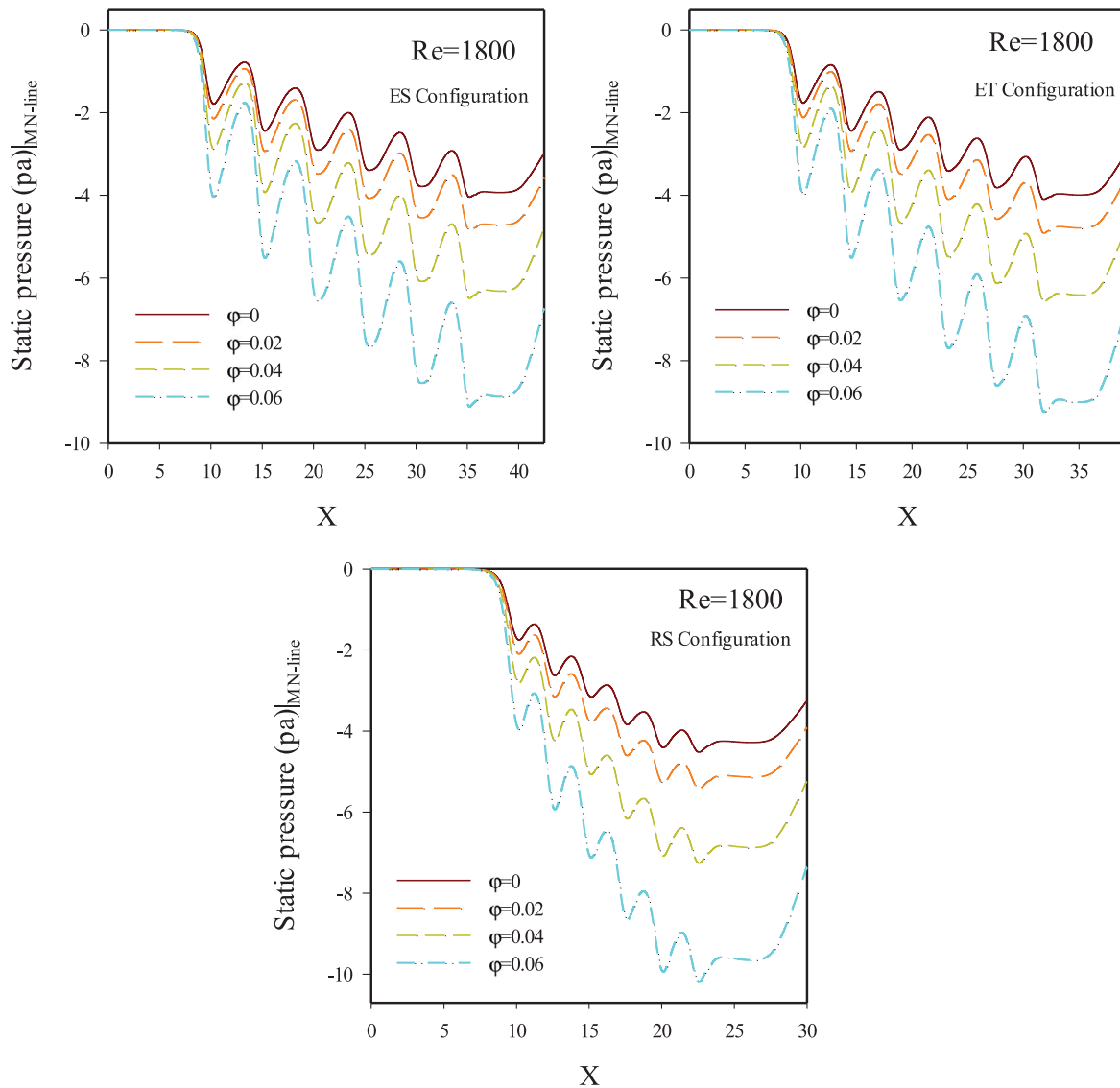
Fig. 12. Changes in static pressure across different Configurations of tube arrays at volumetric fractions of 0–6% of solid nanoparticles at Reynolds 1800.

changes in the static pressure in regions between tubes and for Reynolds 1800. Based on diagrams of Fig. 12, with progression of the fluid between the tube arrays as well as presence of tubes in the motion path of the fluid, the fluid momentum level is depreciated. This behavior shows itself as elevated static pressure. By adding solid nanoparticles in the cooling fluid bed, due to increased viscosity and density of the fluid, the extent of momentum depreciation also increases, such that in investigation of the extent of static pressure drop, the maximum pressure drop across all Configurations is observed at volume fraction 6%, while the minimum pressure drop is seen for pure water fluid. Considering the diagrams of static pressure drop, these diagrams are periodic, i.e. presence of maximum and minimum points in these diagrams is due to changes in the pressure drop in response to fluid motion and the regions before and after the tubes. The minimum regions of the diagram are related to fluid pressure drop in the region ahead of tube arrays, and the maximum regions of the diagram are associated with fluid pressure drop behind the tube arrays. As the fluid velocity reaches zero in response to collision with tube arrays, pressure drop increases significantly. Among the Configurations of tube arrays, it is seen that the maximum static pres-

sure drop in the fluid path is associated with RS Configuration, which is due to placement of tubes within a distance lower than each other. With increase in the distance of tubes from each other, momentum changes of the fluid decrease significantly, thereby diminishing static pressure drop. Following movement of the fluid and passing over the set of tube arrays, the extent of pressure drop diminishes significantly, which is due to passage of fluid over the region of tube sets, whereby due to absence of barrier, static pressure drop diminishes. Across all the diagrams, it is observed that until the length of $X = 10$, all tube Configurations have the same pressure drop equal to zero.

In the diagrams of Fig. 13, changes in pressure drop coefficient on different rows of tube arrays for different Configurations of tube arrays at volumetric fractions of 0–6% solid nanoparticles at Reynolds 100 are observed. Indeed, this factor represents interaction between pressure forces and inertial forces (velocity). Across all the pressure drop coefficient diagrams, it is seen that with the movement of fluid over the tube arrays, the extent of pressure drop diminishes, such that this extent of reduction is evident from the second row onwards. Among the tube arrays placed in the fluid path, the tubes in the
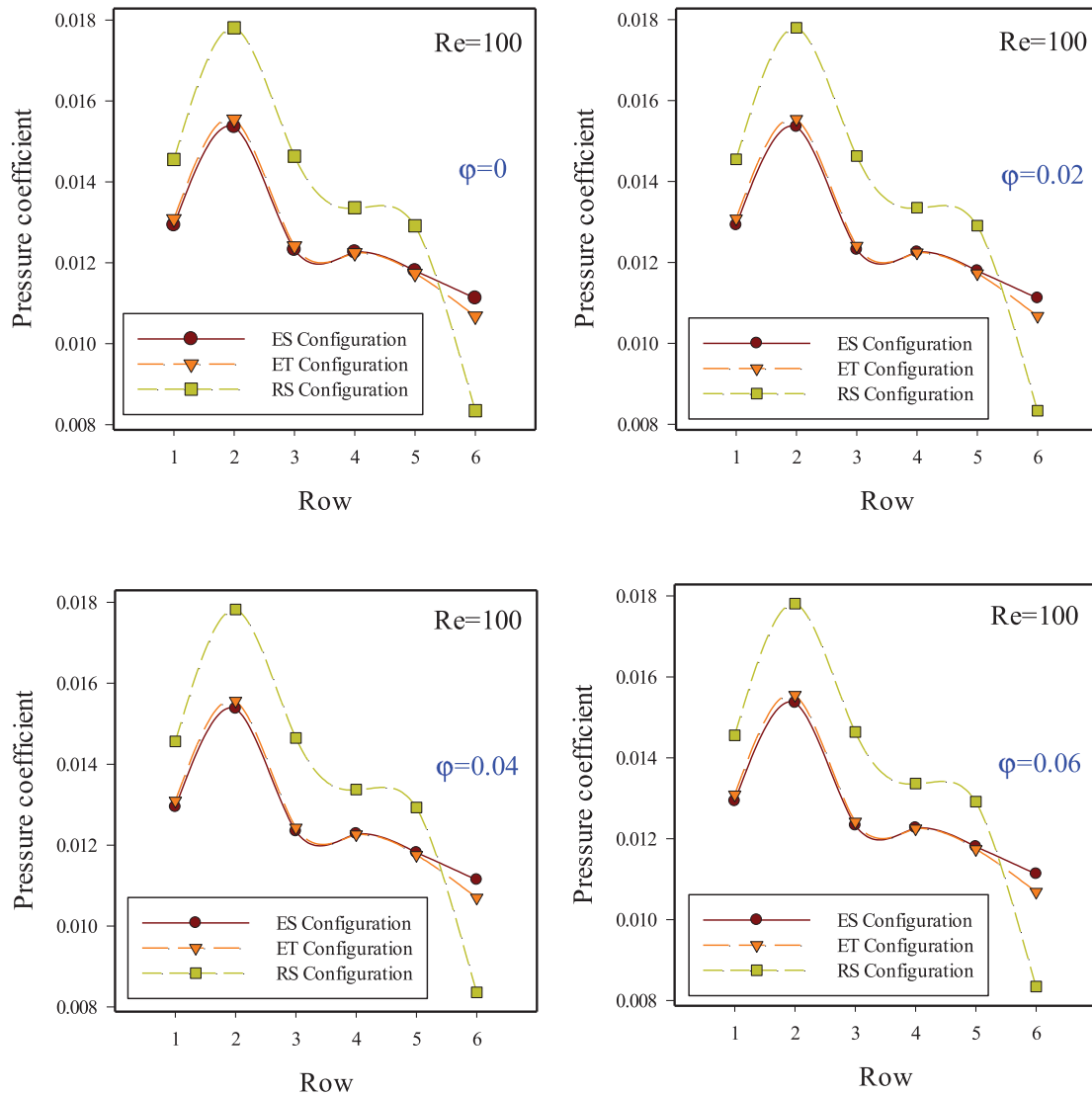
Fig. 13. The diagrams of pressure drop coefficient on the tube arrays across different Configurations of tube arrays at Reynolds 100.

second row have the maximum extent of pressure drop coefficient, while the tubes in the sixth row have the lowest extent of pressure drop.

Across almost all investigated cases, the extent of pressure drop coefficient in the tubes of the first and third rows in RS Configuration is almost the same. As collision of the fluid with the tube arrays of the first row is followed by the maximum momentum, thus inertial force has a more dominant effect in comparison with pressure forces. In the second row, as the momentum of the fluid has diminished when passing over the first row tubes, the pressure forces are more dominant. The pressure drop coefficient at the rows 3, 4, and 5 gradually diminishes with the movement of fluid between the tube arrays, such that from the second group onwards, the extent of inertial forces finds dominant effects in comparison with pressure forces. From the second row onwards, the slope of pressure drop coefficient diagrams is descending. Among the different Configurations of tubes and across all Reynolds numbers investigated, RS Configuration has the maximum pressure drop coefficient. In this type of Configuration, the extent of fluid momentum depreciation is maximum. The extent of changes in dimensionless temperature along MN line has been plotted in diagrams in Fig. 14. This investigation has been done for Reynolds 1000 across different volu-

metric fractions and Configurations of tubes. With the increase in the volume fraction of solid nanoparticles, the value of dimensionless temperature diminishes significantly, signifying dominance of the effects of cold fluid temperature in inner tube regions. This also means that the extent of cooling has a dominant effect against diffusion of the effects of heat flux of surfaces. This behavior has been plotted across all Configurations. In the input region of the path of tube arrays and before placement of position of tubes, as there is no warm surface in the motion path of the fluid, changes in the parameter of dimensionless temperature are zero. With entrance of the fluid to the region of tubes, effects of thermal gradients at layers above warm wall of tubes diffuse, thereby affecting the behavior of dimensionless temperature. The reduction in dimensionless temperature means diminished effects of the thickness of heat boundary layer. Across the investigated volumetric fractions, the behavior of dimensionless temperature at volumetric fractions of zero and 2% is almost the same. However, at 6%, in comparison with 4%, it decreases significantly. The figure of diagrams of dimensionless temperature is periodic. This is due to the motion path of the fluid between the tubes. Affectability of the shape of diagrams by placement of position of tubes in ES Configuration is lowest, when compared with other Configurations.
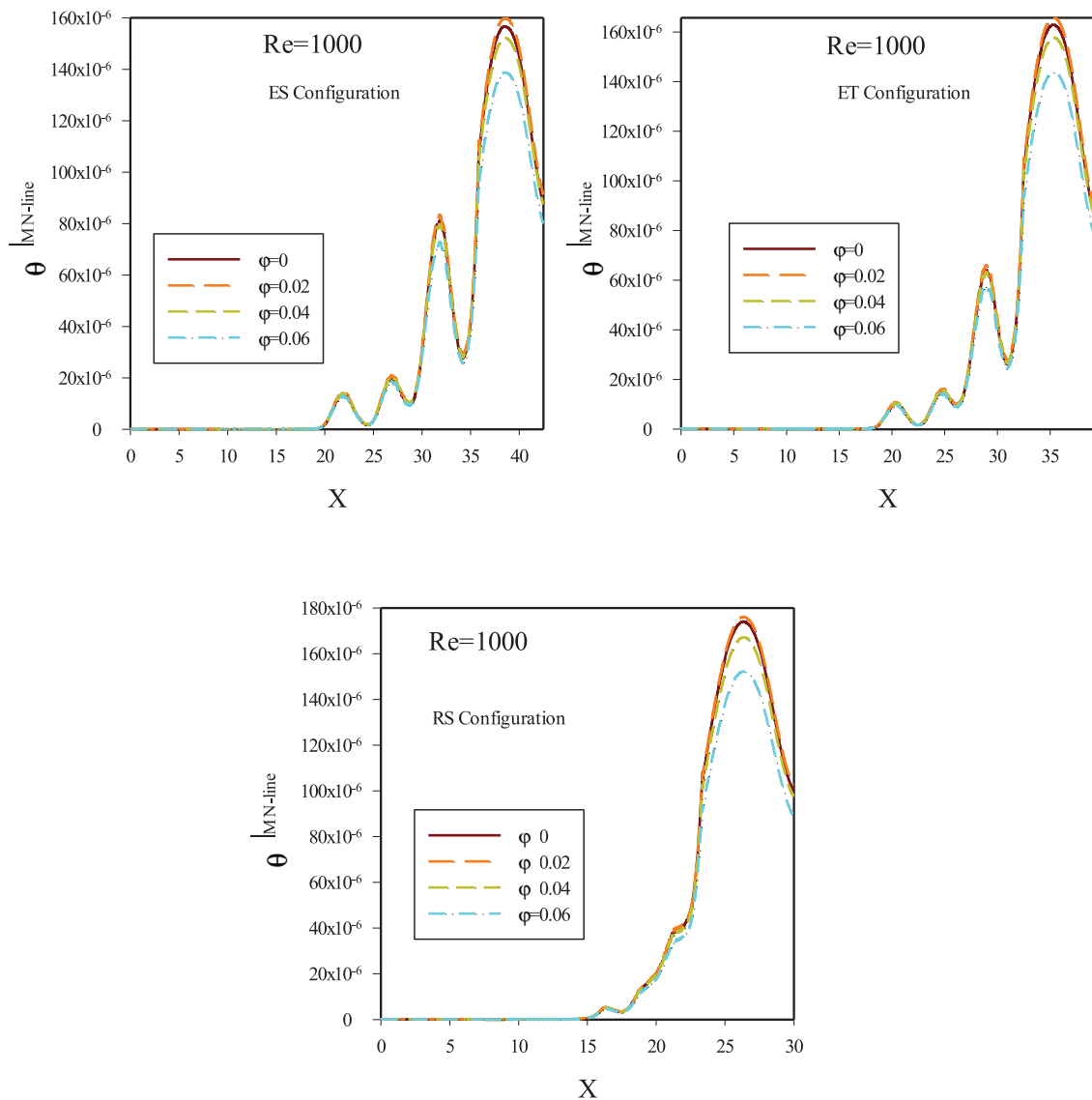
Fig. 14. Changes in dimensionless temperature along MN line at Reynolds 1000.

6. Conclusion

In this research, numerical simulation of laminar flow and heat transfer of nanofluid on tube arrays of heat exchanger with ES, ET, and RS Configurations was described. The heat transfer behavior and laminar flow of two-phase nanofluid as cooling fluid were examined at volumetric fractions of 0, 2, 4, and 6% of solid silver nanoparticles at Reynolds 100, 400, 1000, and 1800. The results of this research indicate that increased volume fraction of solid nanoparticles brings about elevated heat transfer, pressure drop, and friction factor. Among the investigated cases, it is observed that growth of heat boundary layer, temperature changes and the effect of diffusion of warm fluid in RS Configuration is lowest when compared with ET and ES cases, which is due to the type of geometrical Configuration and distance between the tube arrays. Across the examined Configurations, in ES due to the maximum longitudinal distance between the tube arrays, the flow of the fluid faces vortex formation after passing over the tube arrays and gradually the extent of growth of vortexes behind the terminal tube arrays reaches its maximum. Once the fluid passes over 0–120°, the extent of heat transfer diminishes due to changes in the velocity elements on circular surfaces. At 120°, due to separation of the fluid flow off the circular surfaces and the instability of the velocity profile, special changes can be seen in the behavior of local Nusselt number. The fluid motion after 120° due to formation of weak region and vortex mixing of the fluid resulting from pressure drop, at the backside of the tube arrays, brings about increased heat transfer up to 180° Among the investigated diagrams, the level of Nusselt number diagram in RS state has the maximum level, while the minimum belongs to ES. In RS, with increase in the fluid velocity (Reynolds number), Nusselt number diagrams tend to bowl, meaning that elevated velocity of the fluid causes development of strong vortexes behind tube arrays, bringing about better mixing of the fluid.

References

[1] Abedini E, Zarei T, Afrand M, Wongwises S. Experimental study of transition flow from single phase to two phase flow boiling in nanofluids. J Mol Liq 2017;231:11–19.

[2] Abedini E, Zarei T, Rajabnia H, Kalbasi R, Afrand M. Numerical investigation of vapor volume fraction in subcooled flow boiling of a nanofluid. J Mol Liq 2017;238:281–9.

[3] Teimouri H, Sheikhzadeh GA, Afrand M, Fakhari MM. Mixed convection in a rotating eccentric annulus containing nanofluid using bi-orthogonal grid types: a finite volume simulation. J Mol Liq 2017;227:114–26.

[4] Safaei MR, Safdari Shadloo M, Goodarzi MSh, Hadjadj A, Goshayeshi HR, Afrand M, Kazi SN. A survey on experimental and numerical studies of convection heat transfer of nanofluids inside closed conduits. Adv Mech Eng 2016;8(10):1–14.

[5] Goodarzi M, Kherbeet ASh, Afrand M, Sadeghinezhad E, Mehrali M, Zahedi P, Wongwises S, Dahari M. Investigation of heat transfer performance and friction factor of a counter-flow double-pipe heat exchanger using nitrogen-doped, graphene-based nanofluids. Int Comm Heat Mass Transf 2016;76:16–23.

[6] Shahsavar A, Khanmohammadi S, Toghraie D, Salihepour H. Experimental investigation and develop ANNs by introducing the suitable architectures and training algorithms supported by sensitivity analysis: measure thermal conductivity and viscosity for liquid paraffin based nanofluid containing Al2O3 nanoparticles. J Mol Liq 2019;276:850–60.

[7] Shahsavar A, Khanmohammadi S, Karimipour A, Goodarzi M. A novel comprehensive experimental study concerned synthesizes and prepare liquid paraffin-Fe3O4 mixture to develop models for both thermal conductivity & viscosity: a new approach of GMDH type of neural network. Int J Heat Mass Transf 2019;131:432–41.

[8] Liu WI, Alsarraf J, Shahsavar A, Rostamzadeh M, Afrand M, Nguyen TK. Impact of oscillating magnetic field on the thermal-conductivity of water-Fe3O4 and water-Fe3O4/CNT ferro-fluids: experimental study. J Magn Magn Mater 2019;484:258–65.

[9] Kim T. Effect of longitudinal pitch on convective heat transfer in crossflow over in-line tube banks. Ann. Nucl. Energy 2013;57:209–15.

[10] Iwaki C, Cheong K, Monji H, Matsui G. PIV measurements of vertical cross-flow structure over tube bundles. Exp Fluids 2004;37:350–63.

[11] Godson L, Deepak K, Enoch C, Jefferson B, Raja B. Heat transfer characteristics of silver/water nanofluids in a shell and tube heat exchanger. Arch Civ Mech Eng 2013. http://dx.doi.org/10.1016/j.acme.2013.08.002.

[12] Wang YQ, Penner LA, Ormiston SJ. Analysis of laminar forced convection of air for crossflow in banks of staggered tubes. Numer Heat Transf Part A: Appl 2000;38(8):819–45.

[13] Mangrulkar CK, Dhoble AS, Chakrabarty SG, Wankhede US. Experimental and CFD prediction of heat transfer and friction factor haracteristics in cross flow tube bank with integral splitter plate. Int J Heat Mass Transf 2017;104:964–78.

[14] Wang Y, Gu X, Jin Z, Wang K. Characteristics of heat transfer for tube banks in crossflow and its relation with that in shell-and-tube heat exchangers. Int J Heat Mass Transf 2016;93:584–94.

[15] Iacovides H, Launder B, West A. A comparison and assessment of approaches for modelling flow over in-line tube banks. Int J Heat Fluid Flow October 2014;49:69–79.

[16] Mangrulkar CK, Dhoble AS, Deshmukh AR, Mandavgane SA. Numerical investigation of heat transfer and friction factor characteristics from in-line cam shaped tube bank in crossflow. Appl Therm Eng 2016. http://dx.doi.org/10.1016/j.applthermaleng.2016.08.174.

[17] Aminossadati SM, Ghasemi B. Natural convection cooling of a localized heat source at the bottom of a nanofluid-filled cavity. Eur J Mech B/Fluids 2009;28:630–40.

[18] Karimipour A, Alipour H, Akbari OA, Toghraie Semiromi D, Hemmat Esfe M. Studying the effect of indentation on flow parameters and slow heat transfer of water-silver nanofluid with varying volume fraction in a rectangular two dimensional microchannel. Ind J Sci Tech 2015;8(15):51–70.

[19] Alsarraf J, Moradikazerouni A, Shahsavar A, Afrand M, Salehipour H, Tran MD. Hydrothermal analysis of turbulent boehmite alumina nanofluid flow with different nanoparticle shapes in a minichannel heat exchanger using two-phase mixture model. Physica A 2019;520:275–88.

[20] Chon H, Kihm KD, Lee SP, Choi SUS. Empirical correlation finding the role of temperature and particle size for nanofluid (Al2O3) thermal conductivity enhancement. Appl Phys Lett 2005;87:1–3.

[21] Karimi A, Al-Rashed AAAA, Afrand M, Mahian O, Wongwises S, Shahsavar A. The effects of tape insert material on the flow and heat transfer in a nanofluid-based double tube heat exchanger: two-phase mixture model. Int J Mech Sci 2019;156:397–409.

[22] Alipour H, Karimipour A, Safaei MR, Toghraie Semiromi D, Akbari OA. Influence of T-semi attached rib on turbulent flow and heat transfer parameters of a silver-water nanofluid with different volume fractions in a three-dimensional trapezoidal microchannel. Phys E 2017;88:60–76.

[23] Akbari OA, Toghraie D, Karimipour A. Numerical simulation of heat transfer and turbulent flow of water nanofluids copper oxide in rectangular microchannel with semi attached rib. Adv Mech Eng 2016;8(4):1–25.

[24] Maiga SE, Nguyen CT, Galanis N, Roy G. Heat transfer behaviors of nanofluids in a uniformly heated tube. Super Lattices Microstruct 2004;35:543–57.

[25] Goodarzi M, Ahmad A, Mohammad Shahab G, Mohammad Reza S, Karimipour A, Mohseni Languri E, Mahidzal D. Investigation of heat transfer and pressure drop of a counter flow corrugated plate heat exchanger using MWCNT based nanofluids. Int Commun Heat Mass Transf 2015;66:172–9.

[26] Al-Rashed AAAA, Shahsavar A, Entezari S, Moghimi MA, Adio SA, Nguyen TK. Numerical investigation of non-Newtonian water-CMC/CuO nanofluid flow in an offset strip-fin microchannel heat sink: thermal performance and thermodynamic considerations. Appl Therm Eng 2019;155:247–58.

[27] Akbari OA, Karimipour A, Toghraie Semiromi D, Safaei MR, Alipour H, Goodarzi M, Dahari M. Investigation of rib's height effect on heat transfer and flow parameters of laminar water-Al2O3 nanofluid in a two dimensional ribmicrochannel. Appl Math Comp 2016;290:135–53.

[28] Khanafer K, Vafai K, Lightstone M. Buoyancy-driven heat transfer enhancement in a two dimensional enclosure utilizing nanofluids. Int J Heat Mass Transf 2003;46:3639–53.

[29] Behnampour A, Akbari OA, Safaei MR, Ghavami M, Marzban A, Shabani GAS, Zarringhalam M, Mashayekhi R. Analysis of heat transfer and nanofluid fluid flow in microchannels with trapezoidal, rectangular and triangular shaped ribs. Phys E 2017;91:15–31.

[30] Gravndyan Q, Akbari OA, Toghraie D, Marzban A, Mashayekhi R, Karimi R, Pourfattah F. The effect of aspect ratios of rib on the heat transfer and laminar water/TiO2 nanofluid flow in a two-dimensional rectangular microchannel. J Mol Liq 2017;236:254–65.

[31] Safaei MR, Gooarzi M, Akbari OA, Safdari Shadloo M, Dahari M. Performance evaluation of nanofluids in an inclined ribbed microchannel for electronic cooling applications. Electronics cooling. Sohel Murshed Prof S M, editor. InTech; 2016. Available from: http://www.intechopen.com/books/electronics-cooling/performance-evaluation-of-nanofluids-in-an-inclined-ribbed-microchannel-for-electronic-cooling-appli. doi:10.5772/62898.

[32] Akbari OA, Toghraie D, Karimipour A, Marzban A, Ahmadi GR. The effect of velocity and dimension of solid nanoparticles on heat transfer in non-Newtonian nanofluid. Phys E 2017;86:68–75.

[33] Nikkhah Z, Karimipour A, Safaei MR, Forghani-Tehrani P, Goodarzi M, Dahari M, Wongwises S. Forced convective heat transfer of water/functionalized multi-walled carbon nanotube nanofluids in a microchannel with oscillating heat flux and slip boundary condition. Int Commun Heat Mass Transf 2015;68:69–77.

[34] Heydari M, Toghraie D, Akbari OA. The effect of semi-attached and offset mid-truncated ribs and Water/TiO2 nanofluid on flow and heat transfer properties in a triangular microchannel. Therm Sci Eng Prog 2017;2:140–50.

[35] Xia GD, Liu R, Wang J, Du M. The characteristics of convective heat transfer in microchannel heat sinks using Al2O3 and TiO2 nanofluids. Int Commun Heat Mass Transf 2016. http://dx.doi.org/10.1016/j.icheatmasstransfer.2016.05.034.

[36] Safaei MR, Rahmanian B, Goodarzi M. Numerical study of laminar mixed convection heat transfer of power-law non-newtonian fluids in square enclosures by finite volume method. Int J Phys Sci 2011;6(33):7456–70.

[37] Afrand M, Rostami S, Akbari M, Wongwises S, Esfe MH, Karimipour A. Effect of induced electric field on magneto-natural convection in a vertical cylindrical annulus filled with liquid potassium. Int J Heat Mass Transf 2015;90:418–26.

[38] Afrand M, Farahat S, Nezhad AH, Sheikhzadeh GA, Sarhaddi F, Wongwises S. Multi-objective optimization of natural convection in a cylindrical annulus mold under magnetic field using particle swarm algorithm. Int Commun Heat Mass Transf 2015;60:13–20.

[39] Zdravistch F, Fletcher CA, Behnia M. Numerical laminar and turbulent fluid flow and heat transfer predictions in tube banks. Int J Numer Meth Heat Fluid Flow 1995;5:717–33.

[40] Nishimura T, Itoh H, Ohya K, Miyashita H. Experimental validation of numerical analysis of flow across tube banks for laminar flow. J Chem Eng Jpn 1991;24:666–9.

[41] Incropera FP, DeWitt DP. Fundamentals of heat and mass transfer. 4th ed. New York: Wiley; 1996.